Odor representations in the olfactory bulb evolve after the first breath and persist as an odor afterimage

Michael Andrew Patterson[a,b], Samuel Lagier[a,b], and Alan Carleton[a,b,1]

[a]Department of Basic Neurosciences, School of Medicine, University of Geneva, CH-1211 Geneva 4, Switzerland; and [b]Geneva Neuroscience Center, University of Geneva, CH-1211 Geneva 4, Switzerland

Edited by John G. Hildebrand, University of Arizona, Tucson, AZ, and approved July 9, 2013 (received for review March 6, 2013)

Rodents can discriminate odors in one breath, and mammalian olfaction research has thus focused on the first breath. However, sensory representations dynamically change during and after stimuli. To investigate these dynamics, we recorded spike trains from the olfactory bulb of awake, head-fixed mice and found that some mitral cells' odor representations changed following the first breath and others continued after odor cessation. Population analysis revealed that these postodor responses contained odor- and concentration-specific information—an odor afterimage. Using calcium imaging, we found that most olfactory glomerular activity was restricted to the odor presentation, implying that the afterimage is not primarily peripheral. The odor afterimage was not dependent on odorant physicochemical properties. To artificially induce aftereffects, we photostimulated mitral cells using channelrhodopsin and recorded centrally maintained persistent activity. The strength and persistence of the afterimage was dependent on the duration of both artificial and natural stimulation. In summary, we show that the odor representation evolves after the first breath and that there is a centrally maintained odor afterimage, similar to other sensory systems. These dynamics may help identify novel odorants in complex environments.

multielectrode recording | network dynamics | optogenetics

Sensory systems, even when presented with fixed stimuli, use dynamic neural representations that change over time. These changes range from simple potentiation or adaptation to more complex temporal patterns (1, 2). These dynamics can persist even after the cessation of stimulus, which can take the form of an off-response or prolonged aftereffect. Aftereffects have been intensely studied in vision (1, 3) and also observed in audition (4, 5), touch (6, 7), taste (here the afterimages may be due to persistent ligand binding) (8, 9), and insect olfaction (10, 11). In mammalian olfaction, the only reported aftereffect is a "persistent afterdischarge" following high concentration odors (12).

Olfaction is an active process that is coordinated by breathing (2, 13). Odorants bind to odorant receptor neurons (ORNs) in the epithelium, which synapse onto mitral/tufted (M/T) cells in the olfactory bulb (OB) at precisely defined glomeruli. Direct recordings of ORNs in rats show that ORNs are excited by odors and that activity can last for seconds after odor cessation (14). Others have measured the output of ORNs, by imaging glomeruli, and found that the response is gated by each breath and that the amplitude decreases with time (13, 15). The importance of breath segmentation for M/T cells has recently been shown in awake subjects, where neurons respond with precise, phasic firing patterns (16–18). However, these recordings have focused on how information is represented during the first breath, as rodents can identify odors in a single breath (19–21). Activity in piriform cortex is also segmented by breaths, and neurons there respond sparsely (22, 23), and with adaptation (24, 25). To date, no one has addressed, in the OB of awake rodents, how the odor representation evolves with each breath and how the odor representation changes after odor offset. Answering these questions will yield insight into how odor identity is maintained and how the olfactory network represents odors.

To investigate olfactory dynamics, we recorded from M/T cells in awake, head-fixed mice. We found that, during the odor, the odor representation shifts significantly after the first breath and not via simple attenuation. Furthermore, we observed a subset of cells that responded in an odor-specific manner after odor cessation—an olfactory afterimage. We performed calcium imaging on sensory neuron terminals, photostimulated channelrhodopsin-expressing M/T cells, and determined that the afterimage is primarily maintained centrally rather than peripherally. In conclusion, we have found that the odor response is dynamic and that one must consider all breaths of the response during an odor and afterward to characterize a cell's "odor receptive field." The existence of an odor afterimage shows that afterimages may be a general, useful property of all sensory systems.

Results

Evolution of the Odor Representation in Single Cells. We recorded from M/T cells of awake, head-fixed mice, using tetrode arrays, and measured respiration using a directional airflow sensor (average breath duration 327 ± 140 ms, SD; early trials with "fast-sniffing" were elided). We presented odorants (5% dilution in air) to the mice using a custom olfactometer for 2 or 2.5 s, with odor onset timed to follow the end of inspiration. Given the variability of breath duration in awake animals, we aligned each response by truncating spikes that arrive later than the mean breath duration and padded short breaths with empty time. This procedure ensures keeping the actual spike time unaltered for each breath (*Materials and Methods*).

Following realignment, many cells showed clear odor responses with precise firing within the sniff cycle (16, 17). Fig. 1*A* shows a cell with a low basal firing rate that is excited by odor presentation (*Top* and *Middle*), with most spikes coming 100–200 ms after inspiration onset (*Bottom*). This cell continued to fire at the

Significance

Even when presented with steady stimuli, sensory systems respond dynamically, including adaptation or responses after the stimuli are gone (afterimages). To measure these dynamics in smell, we recorded electrical signals from the mouse brain. We found that the neuronal representation of odors changes between breaths, and not by simple adaptation, showing that the olfactory system also undergoes these dynamics. After the end of the odor, the brain continued responding, showing that there are olfactory afterimages. Finally, we tried to isolate where afterimages are generated and found that, while the nose has some contribution, afterimages are mainly maintained in the brain.

Author contributions: M.A.P. and A.C. designed research; M.A.P. and S.L. performed research; M.A.P. and S.L. analyzed data; and M.A.P. and A.C. wrote the paper.

The authors declare no conflict of interest.

This article is a PNAS Direct Submission.

[1]To whom correspondence should be addressed. E-mail: alan.carleton@unige.ch.

This article contains supporting information online at www.pnas.org/lookup/suppl/doi:10.1073/pnas.1303873110/-/DCSupplemental.

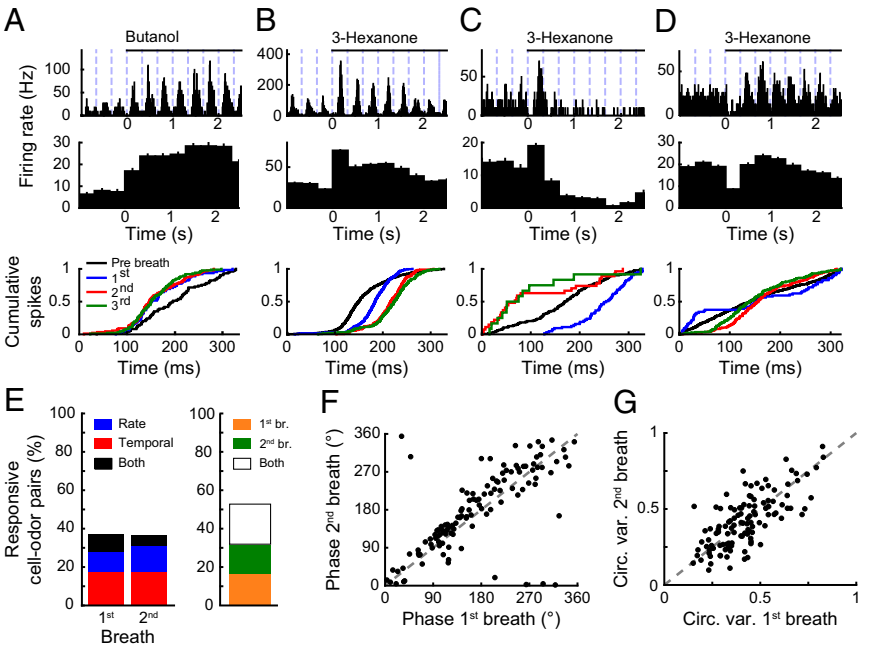

Fig. 1. The odor response of individual cells changes after the first breath. (*A*) This cell fires with the same phase for each breath in response to butanol (5% diluted in air). (*Top*) Histogram of odor response (bin = 20 ms). Inspiration onset marked by dashed blue lines, and odor above. (*Middle*) Average firing rate during each breath. (*Bottom*) Cumulative spike plot during the preodor and first–third odor breaths. (*B*) This cell shifts phase between the first and second odor breath, as seen in *Bottom* cumulative spike plot (KS, $P < 0.02$). (*C*) This cell is excited for one breath before being inhibited (ANOVA, $P < 0.05$). (*D*) This cell is inhibited for the first breath before firing phasically (ANOVA, $P < 0.05$). (*E*) Percentage of responsive cell-odor pairs for first and second breath (*Left*). Percentage of cells that respond exclusively during the first or second breath, or respond to both (*Right*). $n = 516$ cell-odor pairs from 10 mice. (*F*) Phase (circular mean) of responses during the first and second breath. The second breath response arrives later. $n = 117$ cell-odor pairs. (*G*) Magnitude of phasicness (circular variance) of response during first and second breath. There is no difference between the first and second breath. Same data as in *F*.

same time for each subsequent breath. In addition to the cells that maintained their response for each breath, a subset of cells changed their odor response after the first breath. The cell in Fig. 1*B* fired phasically during all breaths but fired ∼40 ms later during the second breath than during the first (*Bottom*). Other cells' responses changed more dramatically: some were excited for the first breath before being inhibited (Fig. 1*C*) or were inhibited for just the first breath (Fig. 1*D*). Overall, we saw diverse changes in M/T cells' odor responses between the first and second breath.

To quantify how cells responded, we calculated whether cells exhibit a rate or a temporal change during each breath. To identify rate responses (changes in firing rate during the odor), we averaged for each breath the firing rate over the entire breath and compared this rate with the average baseline firing rate (Fig. 1 *A–D*, *Middle*; ANOVA with Tukey's post hoc test, $P < 0.05$). Of the 516 cell-odor pairs analyzed for Fig. 1, 21% (44 excited, 66 inhibited) responded with a rate change during the first breath, and 19% (36 excited, 61 inhibited) during the second breath (Fig. 1*E*). To detect changes in spike timing (i.e., a temporal change), we calculated the cumulative spike distribution over the breathing cycle (Fig. 1 *A–D*, *Bottom*) for baseline breaths (black line), the first odor breath (blue line), and subsequent breaths (red, green). We tested whether the spike distributions were different using a Kolmogorov–Smirnov (KS) test (*Materials and Methods*). Using this criterion, we found that 27% (137/516) of cell-odor pairs responded during the first breath, and 23% (118/516) responded during the second breath (Fig. 1*E*). Combining these two measurements, we found that 37% (193/516) of cell-odor pairs responded during the first breath with either a rate or temporal change, and 36% (187/516) responded during the second breath (Fig. 1*E*). These response percentages are similar to those observed previously (25% at 0.05% dilution in ref. 16; 60% at 2% dilution in ref. 17). Given that some cells do not respond during the first breath, but respond afterward, we calculated how many cell-odor pairs responded during the first breath alone (16%, 85/516), second breath alone (15%, 79/516), or both (20%, 108/516; Fig. 1*E*). Of the subset of cells that have a temporal response during the first and second breath, 23% (45/192; KS, $P < 0.02$) of cell-odor pairs changed phase between the first and second breath.

To more closely examine these temporal responses, we used circular statistics. For all cells that had both a temporal response and phasic firing during the first and second breath, we calculated the circular mean of firing (i.e., phase) during the breath. Responses during the second breath came, on average, 30 degrees (∼30 ms) later than the first breath (158 ± 6 vs. 190 ± 7 degrees; Watson–Williams test, $P < 0.05$; Fig. 1*F*). We also calculated the circular variance (magnitude of phasicness) for the first and second breath and found no systematic shift in the strength of the phasing (paired t test, $P = 0.27$; Fig. 1*G*). What happens to the odor representation beyond the second breath? We repeated the circular mean test for the second and third breaths and found that the changes in phase were smaller than those between the first and second breath (χ^2 test, $P < 0.01$). In conclusion, the odor representation becomes more stable after the first breath.

These dynamics could have been the result of an unstable stimulus. To characterize our pulse of odorants, we recorded the odor concentration, using a photoionization detector (PID), and performed multiunit recordings on the same day. The PID measurements showed that the concentration reached 80–90% of its final concentration within 150 ms (before the first inspiration), then gradually increased over a few hundred milliseconds (Fig. S1 *A* and *B*). The percentage of responsive cells and changes between breaths were similar for these new measurements compared to our first dataset (Fig. S1*C*). Seeing that the concentration could change 5–10% between the first and second breath, we were

concerned that the representation change between these breaths was due to concentration and not neural dynamics, as these changes are near the intensity discrimination threshold for rats (26). Previous investigations into concentration coding in olfaction have looked at changes in concentration of orders of magnitude, not a few percent (27–29). Given that the concentration changes over the time range of the first breath, we used the variability in breathing as a proxy for small changes in odor concentration (Fig. S1 *D* and *E*). We found similar responses for short and long odor durations before the first odor breath, evidence that the changes between breaths are not due to small concentration changes, but representation dynamics.

Evolution of the Population Representation. We next turned to the population level to see how the ensemble representation changed with each breath. We constructed a population vector that includes each cell's response for the entire breath (Fig. 2*A*) (27) and calculated the distance between the odor representations for each breath (*Materials and Methods*). We found that all odor breaths are different from control breaths (ANOVA, $P < 0.01$; Fig. 2*B*, top row). Furthermore, we found that the first odor breath was different from each subsequent breath whereas all of the later breaths were similar to each other (ANOVA, $P < 0.05$; Fig. 2*B*, second row). On the population level, the odor representation changes the most between the first and second breaths. We found similar results in the experiments following PID measurement (Fig. S1*F*).

As an alternative look at the population, we used a classifier to see whether population activity of individual trials could predict the odor. To do so, we calculated the distance between the population vector for a single trial (sample) and the average population vector of each odor (template); the smallest distance is the "predicted" odor (*Materials and Methods*). Using the same breath for both sample and template, the predictor is at chance during the preodor period and is able to accurately classify the odor for all odor breaths (Fig. 2*C*). As a second measure of how the odor representation evolves, we asked the predictor to classify odor responses using the first or fifth odor breath as a fixed template. Using the first breath as a template, the prediction is most accurate for the first breath but quickly diminishes (Fig. 2*C*); in contrast, using the fifth breath as a template yields a poor prediction for the first breath that improves with each breath (Fig. 2*C*). The fact that these cross-breath predictions are above chance probably reflects the subset of cells that have stable representations for each breath.

Olfactory Representations Following Odor Cessation. In all other sensory systems, aftereffects have been observed both neurally and behaviorally (1, 3–9). To investigate odor coding after odor cessation, we analyzed cells' postodor firing. Some cells that responded to the odor continued to do so after the odor ceased, as if the odor was still present (Fig. 3*A*). Other cells fired phasically, but at a different phase from either preodor or odor firing (Fig. 3*B*). Many cells responded either with prolonged inhibition (Fig. 3*C*) or excitation (Fig. 3*D*). To see whether odor remained after the presentation, we measured the concentration using a PID. Trace odorant remained for a few hundred milliseconds after the stimulus (Fig. S2*A*); thus, for all statistics, we used the fourth postodor breath, which occurs ∼1 s after the end of the odor pulse, after the odor dissipated. Of all cell-odor pairs, we found that 30% of cells had a postodor response that differed from preodor firing (rate, 55/465; temporal, 73/465; both rate and temporal, 12/465; Fig. 3*E*, *Left*). The rate change during postodor responses was toward decreases in firing rate (55/85 decreased; 30/85 increased), similar to the odor responses. Thirty-four percent (158/465) of cell-odor pairs responded only during the odor, 20% (94/465) responded both during the odor and after, and 10% (46/465) responded only during the postodor (Fig. 3*E*, *Right*). To look at the phase of the postodor responses, we compared postodor responses to those during the odor (using odor breath 4 for comparison). The postodor breaths had an earlier phase than odor breaths (Watson–Williams test, $P < 0.01$). The circular variance of postodor responses was higher than the odor responses (paired *t* test, $P < 0.01$; Fig. S2*B*).

The postodor responses could contain information regarding the presented odor or could be a general reset response. To differentiate between these possibilities, we used our odor predictor to investigate the postodor breaths. Here, the predictor was able to correctly identify the presented odor above chance for >10 breaths (or >3 s), after the odor has dissipated, and gradually returned to baseline (Fig. 3*G*). To see whether the postodor representation is similar to the odor representation, we used the fifth odor breath as a template and found that the predictor was only above chance for a few breaths (ANOVA, $P < 0.05$; Fig. S2*C*). To look at the network evolution of the odor afterimage, we performed the breath distance analysis and found that the representation changes gradually with each breath (Fig.

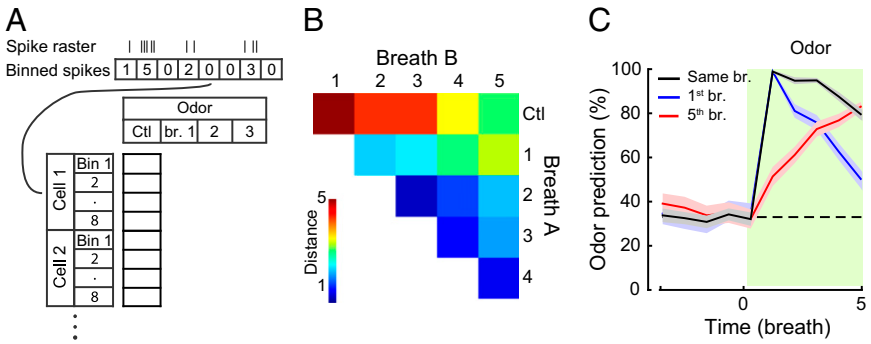

Fig. 2. The population representation changes after the first breath. (*A*) Diagram of population vector construction. Each cell's firing rate was calculated during eight bins (*Top*, ∼40 ms) for each breath before and during the odor. A population vector was then made containing every cell's whole-breath representation for each breath and odor. (*B*) We calculated the distance between preodor (Ctl) and odor breaths (1–5) for each odor and normalized to ctl–ctl distances. The preodor breaths were highly distant from all odor breaths (top row). The first odor breath was also distant from the second–fourth odor breaths (second row). However, the distance between odor breaths 2–5 was similar to the ctrl-ctrl distance. $n = 345$ cell-odor pairs (115 cells from six mice). Color bar: interbreath distance normalized to control breaths. (*C*) Odor prediction using a template from the same breath (black), first odor breath (blue), or fifth odor breath (red) (mean ± SEM of 50 permutations; $n = 124$ cells from five mice). Using the same breath as the template, the prediction was high for all breaths. Using the first or fifth breath as the template yielded accurate predictions only for nearby breaths.

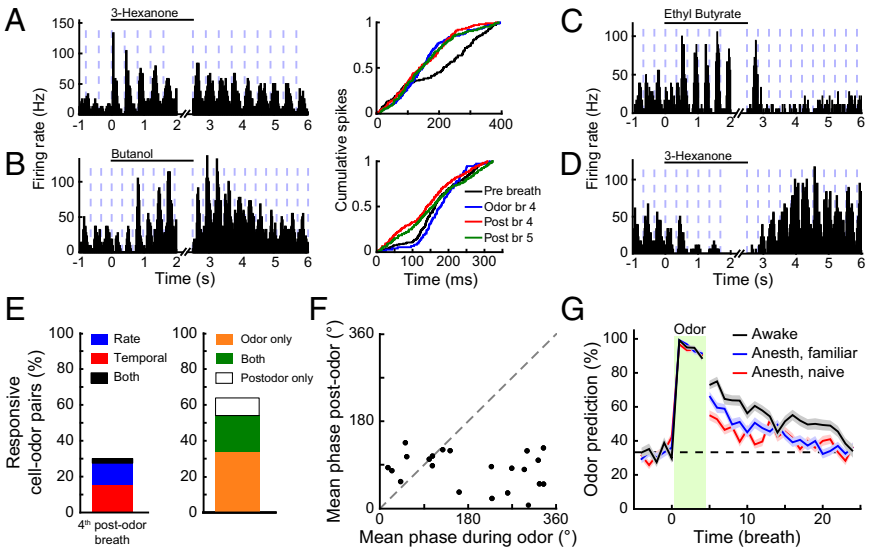

Fig. 3. Individual cells contain odor-specific information after odor offset. (*A*) This cell fires phasically during the odor and postodor. (*Left*) PSTH (bin = 20 ms) during odor and afterward. The odor response was cut at 2 s to allow alignment of the first postodor breath. (*Right*) Cumulative spike plot of the preodor breath (black), fourth odor breath (blue), and the fourth and fifth postodor breaths (red, green). This cell maintains its phase during the postodor. (*B*) This cell fires phasically during the postodor, but with an earlier phase than the preodor or odor firing. (*C*) Histogram of a cell that fires phasically during the odor, but it is inhibited during the postodor. (*D*) Histogram of a cell that is inhibited during the odor and is excited postodor. (*E*, *Left*) Approximately 30% of cell-odor pairs respond during the postodor period (compared with preodor). All statistics were calculated using the fourth breath to avoid lingering odor contamination. (*Right*) Thirty-four percent of cell-odor pairs respond during the odor, 20% respond during both the odor and postodor, and 10% respond only during the postodor (n = 465 cell-odor pairs from 10 mice). (*F*) Phase of responses during the fourth odor breath and fourth postodor breath. The phase of responses is earlier during the postodor (n = 22 cell-odor pairs). (*G*) The ensemble contains odor-specific information after odor cessation. The odor was predicted using the same sample breath as the template (mean ± SEM of 50 permutations; *Materials and Methods*). The odor prediction was higher for awake mice than anesthetized, and, in anesthetized mice, for familiar odors over naïve odors (ANOVA, $P < 0.05$; n = 124 cells from six mice for awake; 168 cells from four mice for familiar; 194 cells from seven mice for naïve).

S2*D*). Furthermore, if we used the odor predictor with a fixed postodor breath template, the prediction was accurate only around the template breath (Fig. S2*C*). Thus, the postodor representation contains odor-specific information, is not a recapitulation of the odor representation, and gradually dissipates. Given these three properties, we propose that the postodor response is an olfactory afterimage.

So far, we have performed all of the experiments in awake mice, but temporal dynamics in other systems have been shown to be dependent on animal state, such as wakefulness or attention (30, 31). To see whether these top-down processes can influence the odor dynamics, we repeated the experiments in anesthetized mice, under two conditions: mice that were presented the odor while awake, and then anesthetized (familiar); and mice that were anesthetized before odor presentation (naïve). In anesthetized mice, the odor representation had interbreath dynamics similar to awake mice (Fig. S3*A*), and individual cells had postodor responses (Fig. S3*B*). After odor cessation, both familiar and naïve mice had postodor predictions above chance, but less than the awake prediction (ANOVA, $P < 0.01$; Fig. 3*G*). The familiar postodor prediction was also higher than the naïve prediction, although only for the first few postodor breaths (ANOVA, $P < 0.05$).

Olfactory Afterimages at Low Concentration. All experiments performed so far were at a high odor concentration (5%), which evokes relatively dense activity patterns in glomeruli (28, 32). To check whether olfactory afterimages are present at lower concentrations, and to see whether the afterimages contain concentration-specific information, we repeated our experiments using three lower odor concentrations (0.1%, 0.4%, and 2%). Individual cells had postodor responses that were concentration-specific (Fig. 4*A*). Postodor responses were present at all concentrations tested, with more postodor responses at the highest concentration (Fig. 4*B*). To investigate concentration coding on the population level, we used the predictor to classify both the odor and concentration presented. During the odor, the predictor was able to identify the odor and concentration with >60% accuracy (Fig. 4*C*). After odor cessation, the predictor was still able to identify the odor and concentration combination above chance for >10 breaths. To ensure that the predictor was working even at the lowest concentration, we used the predictor to classify the odor within each concentration (Fig. 4*D*) and found that it was above chance at all concentrations. We next used the predictor to classify the concentration for each odor. Here, the classification success rate was lower than for odor prediction [because odor representations are similar for different concentrations (27, 33)] but was above chance both during and after the odor (Fig. 4*E*). The experiments at different concentrations allowed us to perform some controls. To see whether the interbreath dynamics are due to the high concentration used, we performed the breath-distance analysis on responses to 0.1% odor and found that the representation changes after the first breath (Fig. S4*A*). To see whether the postodor predictions were simply due to remaining odorant, we predicted postodor breaths using low-concentration odor templates (Fig. S4*B*). These templates were only above chance for a few breaths, like the same-concentration odor template, showing that the afterimage is not simply a low-concentration representation.

Site of Generation of the Olfactory Afterimage. Some possible sources of the postodor responses include lingering input from ORNs, resonant activity within the OB, or feedback from higher order areas. Recordings of ORN activity in anesthetized rats have shown that activity can continue for a few seconds after odor cessation (14). To investigate postodor ORN activity, we performed calcium imaging of sensory terminals in awake, head-fixed OMP-GCaMP3 mice. During odor application, we were able to identify individual

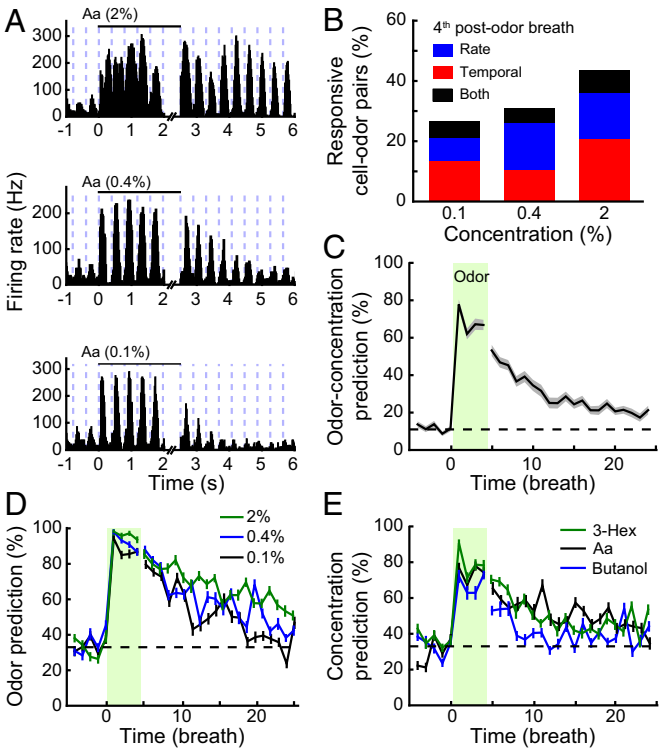

Fig. 4. Postodor responses contain both odor and concentration information. (*A*) PSTHs (bin = 20 ms) from a cell that responds to amyl acetate (Aa) differently at different concentrations (odors diluted first to 10% in mineral oil, then to the final concentration in air). Breaths shown as dashed blue lines. (*B*) Percentage of responsive cell-odor pairs for the fourth postodor breath at each concentration (n = 107 cells from two mice). Same criterion as Fig. 3*E*. (*C*) The population can predict the odor and concentration during both the odor and the postodor period (mean ± SEM of 50 permutations, chance level = 11%). (*D*) The odor and postodor prediction is present at all concentrations (mean ± SEM of 50 permutations, chance level = 33%). (*E*) The postodor prediction contains concentration information for all odors (mean ± SEM of 50 permutations, chance level = 33%).

glomeruli that responded to the stimulus (Fig. 5*A*). Like M/T-cell activity, calcium responses in glomeruli are gated by breaths, with sharp increases in fluorescence following inspiration (Fig. 5*B*). Following odor cessation, the fluorescence in most glomeruli decayed with a single monotonic exponential. However, in a small minority of glomeruli, breath-by-breath activity continued for a few seconds after odor cessation (Fig. 5*B*, *Center*, top trace).

To quantify the responses, we calculated the normalized change in fluorescence (ΔF/F) during each breath for responsive glomeruli–odor pairs (Fig. 5*C*). The responses were largest during the first breath, as the signal had increased from baseline. Following odor offset, the ΔF/F returned to baseline in a few breaths. For glomeruli that respond to at least one odorant, we then calculated for each breath the percentage of glomeruli that showed a response above noise level (Fig. 5*D*). During the odor, ∼65% of the glomeruli responded during the first breath, and this percentage diminished with each breath. Following odor offset, by the fourth breath, ∼95% of the glomeruli stopped responding. We should note that this is not a precise estimate of glomeruli responsiveness: we are not considering glomeruli that did not respond to any odor; have selected odorants that activate the dorsal surface; and are missing glomeruli that are below the sensitivity of the calcium indicator. To enable more direct comparison of the imaging results to the electrophysiology, we used the odor predictor, this time building populations out of glomeruli activity. The predictor was able to identify the odor with >80% accuracy during the first breath, and >50% accuracy for all breaths (Fig. 5*E*). However, during the postodor period, the predictor was accurate only for a single breath. Although a small fraction of sensory neurons do respond after odor cessation, they do not appear to contain as much odor-specific information as M/T cells.

Odorant properties such as polarity, volatility, and sorptiveness can affect how quickly odorants are absorbed into the epithelium and have been shown to affect olfactory bulb activity and behavior (34–36). To see whether these properties could influence the odor afterimage, we repeated the experiments using odorants with a wide range of physicochemical properties. For both imaging and electrophysiology, we quantified the percentage of regions of interest (ROIs) or cells that responded during the fourth postodor breath for individual odors and plotted this percentage against odorant polarity, volatility, and sorptiveness (Fig. 6). There was no significant effect of any of these properties.

If the odor afterimage is not maintained peripherally, it must be maintained centrally. To try to observe the central representation, we recorded from the OB in the absence of peripheral

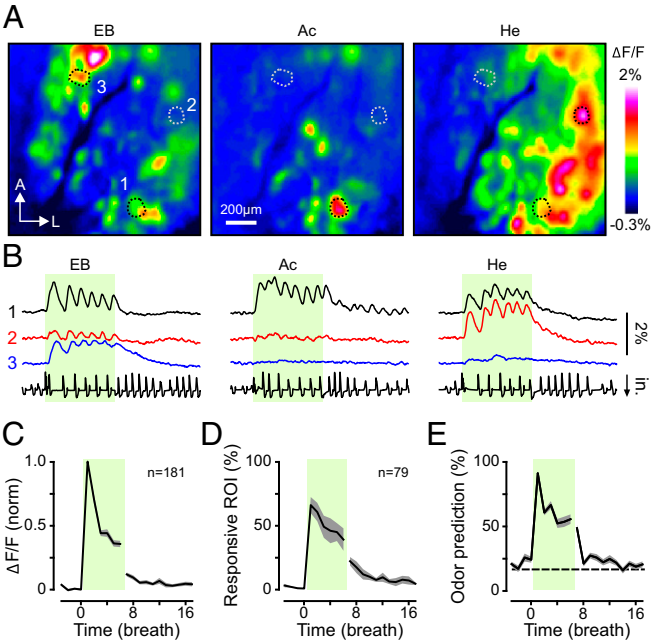

Fig. 5. Sensory activity is nonpersistent after odor cessation. (*A*) Average olfactory maps obtained for three odorants (Ac, acetophenone; EB, ethylbutyrate; He, 3-Hexanone) in the same awake mouse. The fluorescence from GCaMP3, expressed under the control of the olfactory marker protein (OMP) promoter, is averaged over the 3 s of odor presentation and is represented as ΔF/F. (*B*) Calcium dynamics in sensory neuron terminals from the ROI drawn in *A*, for individual trials. The breathing of the animal is presented in the lower trace. The *Center* black trace (ROI 1, acetophenone) shows a rare example of a cycle-by-cycle modulation of the fluorescence signal after the end of the odor presentation. All of the odorants are diluted 20× in air and are presented for 3 s. (*C*) Normalized responses from glomeruli–odor pairs that respond to odor (n = 181). The amplitude of the fluorescence is measured for each breath and normalized to the amplitude of the first breath during the odor presentation (nyanza green box). A single exponential decay was fitted to and removed from the postodor data. The area around the curve represent ± SEM. (*D*) Average fraction of glomeruli that respond to a stimulus. For all six odorants, we calculated the percent of glomeruli that responded, including all glomeruli that responded to at least one odorant (n = 79 glomeruli). (*E*) Prediction of odor identity based on sensory inputs. Using a population vector consisting of all glomeruli that respond to an odor (n = 79 glomeruli), we predicted the odor during and after presentation. The predictor is able to identify the odor during presentation but returns to chance quickly afterward. Mean ± SEM of 50 bootstrapped samples using 50 glomeruli.

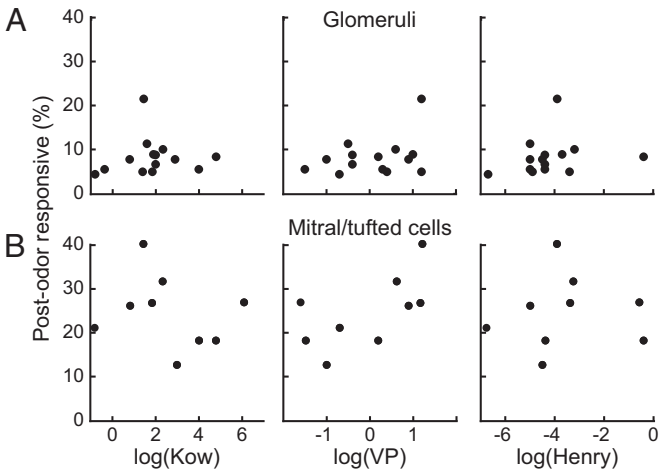

Fig. 6. Odor physicochemical properties do not affect the odor afterimage. (*A*) Percentage of imaged ROIs with a postodor response during the fourth postodor breath, plotted as a function of polarity [water-octanol partition, log(K_{ow})], vapor pressure (VP; log of VP in mmHg at 25 °C), and sorbptiveness (log of Henry's law constant). No property was significantly correlated with postodor responsiveness (linear fit; K_{ow}, $P = 0.54$; VP, $P = 0.2$; Henry, $P = 0.92$). For odorants and physicochemical properties see Table S1. (*B*) Percentage of cell-odor pairs with postodor response during the fourth postodor breath (including both rate and temporal responses). No property was significantly correlated with postodor responsiveness (linear fit; K_{ow}, $P = 0.55$; VP, $P = 0.08$; Henry, $P = 0.86$).

input by blocking the nostril ipsilaterally to the recording site. To block the nostril, we applied a liquid silicone elastomer around the nostril and let it harden. Mice were anesthetized to reduce stress and to prevent them from removing the block. When we applied the plastic, the air pressure measured from the contralateral nostril doubled (Fig. 7 *A* and *B*).

With the nostril blocked, we recorded spikes from M/T cells (layer verified by odor responses after elastomer removal). Blocking the nostril nearly silenced neurons (37). When we applied odorants, only 4/423 cell-odor pairs responded during the first breath, showing that feedback alone is insufficient to drive OB activity for almost all neurons (38).

We also measured the local field potential (LFP) from the mitral cell layer, which allowed us to record subthreshold activity from both mitral and granule cells (39). At rest, with the nostril open, breathing induced theta-frequency deflections, and odors elicited gamma oscillations (Fig. 7 *A* and *C*) (40). In contrast, at rest, nostril blockade reversed the polarity of inspiration deflections and decreased the LFP power at all frequencies (Fig. 7 *B* and *D*). With the nostril blocked, odor presentation still caused theta and gamma activity in the LFP, despite lacking direct ORN input (Fig. 7*B*); the large inspiration-induced deflection was delayed ~50ms. To quantify these changes, we calculated the LFP power for 3–4 s before, during, and after the odor. At some recording locations, with the nostril blocked, the LFP power at frequencies between 5 and 30 Hz increased both during the odor and during the postodor period (Fig. 7*C*). These frequencies are consistent with those for cortical feedback (40, 41). We averaged the LFP power from nine recording sites and found that, with the nostril blocked, the LFP power during the odor and postodor period was higher than the preodor period (Fig. 7*D*). One possible site of the odor afterimage is in the connectivity between the OB and olfactory cortices.

If the odor afterimage is maintained centrally, we wondered whether it would be possible to artificially stimulate the network and generate persistent activity without ORN input. We recorded from M/T cells in the medial OB of awake Thy1-ChR2 mice (42) and placed a light fiber coupled to blue laser (473 nm, 10–15 mW, 2-ms pulses) just above the dorsal surface of the OB, >1 mm away. However, when we flashed the light, the mice salivated and became agitated, making stable recording impossible. In the one awake mouse that we tried to record, light stimulation of more than one pulse induced fast sniffing (resting rate, 2.85 ± 0.7 Hz prelight; one pulse, 2.83 ± 0.57 Hz; >5 pulses, 6.3 ± 1.6 Hz; mean ± SD). Therefore, we shifted to anesthetized mice. We stimulated the OB at 10 or 20 Hz for 0.1–2.5 s. Light stimulation did not change the breathing rate in anesthetized mice (prelight, 2.58 ± 0.12 Hz; postlight, 2.77 ± 0.16 Hz). Following a single light pulse, the M/T cells' firing was basically unaffected. Each light pulse caused large deflections in the LFP (Fig. 8*A*). Following stimulation for more than 0.5 s, many M/T cells exhibited persistent firing that could last seconds (Fig. 8*B*); other cells underwent prolonged inhibition (Fig. 8*C*); and some cells were unaffected

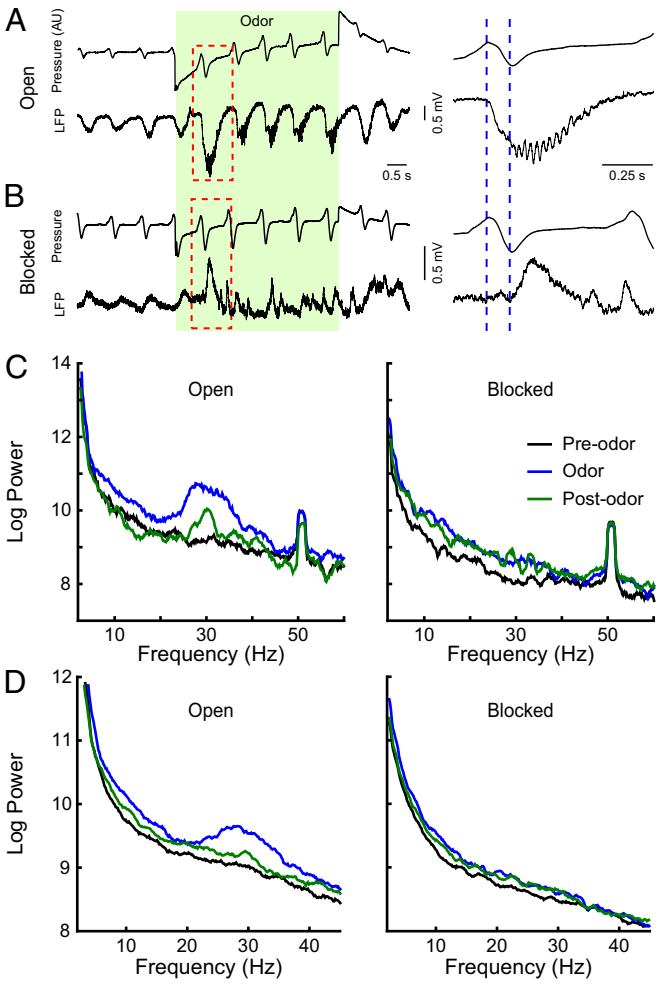

Fig. 7. Odor evokes activity in OB when the ipsilateral nostril is blocked. (*A* and *B*) Example air pressure (*Upper*) and LFPs (*Lower*) from open (*A*) and closed (*B*) nostril. Inspiration is up. Blocking the nostril causes inspiration-induced LFP deflections to change polarity. For both the open and blocked nostril, odor presentation increases LFP activity. (*C*) Power spectrum for the LFP shown in *A* and *B*. The power was calculated over 3- to 4-s epochs before, during, and after the odor. (*D*) Average power of all locations for open and blocked nostril ($n = 9$ recording sites from three mice). The power was higher during the odor and postodor than during the preodor (two-way ANOVA with factors of frequency and odor condition, $F_{odor\ (2,12)} = 5.19$, $P < 0.05$ for odor factor; odor vs. preodor, $P < 0.05$ with least significant difference post hoc test; odor vs. postodor, $P < 0.05$). The frequency was taken as the mean frequency of each recording at 5, 10, ..., 35 Hz).

(Fig. S5*A*). We were often unable to record spikes during the light trains, either due to the large LFP changes making spike extraction difficult, or due to the M/T cells being silenced by inhibitory activity in the network. Photostimulation of wild-type mice yielded neither LFP fluctuations nor persistent firing (Fig. 8*D*).

To quantify the change in firing rate, we calculated the difference between the firing profile for prelight control breaths and postlight breaths (Fig. 8*D*; *Materials and Methods*). At 10 Hz, increasing the stimulus duration caused longer and stronger firing changes. Furthermore, for stimuli longer than 1 s, higher stimulation frequency caused larger firing differences. To better look at the duration of the effect, we calculated the firing difference breath-by-breath for each firing condition (Fig. S5*B*). At 10 Hz, the effect lasted only a few breaths whereas, at 20 Hz, the effect lasted >10 breaths.

Given that longer artificial stimulation yielded longer network activity, we asked whether natural stimuli could do so as well and varied olfactory drive by presenting odors to awake mice for 0.5–5 s. We found that some M/T cells' postodor responses differed between short and long odor application (Fig. 8*E*). On the population level, we used the odor predictor to classify postodor responses and found that the predictor was more accurate following longer odor application (ANOVA, $P < 0.05$; Fig. 8*F*). We measured the postodor odorant concentration using a PID and found that the concentrations were basically identical following different length odor presentation; thus, the improved postodor accuracy is not due to increased odorant concentration (Fig. S6*A*). In insects, following odor application of different lengths, the network returns to baseline via a common trajectory (10). To compare postodor trajectories, we calculated the distance between the postodor representation following 2 s and 5 s odor application (Fig. S6*B*). These representations were highly different, perhaps reflecting that the network responsible for the postodor effect had not settled into a fixed state. The long odor presentation also allowed us to compare the decrease in information during the odor to the decreases during the postodor (Fig. S6*C*). The breath-by-breath decrease in information was more variable between breaths during the afterimage, perhaps due to the smaller number of informative cells, but the magnitudes were similar. In summary, driving the OB network more strongly, either via natural or artificial stimulation, enhances persistent network activity.

Discussion

Although it has been shown that the sniff cycle is integral to the odor code, no one has focused on how the odor code changes

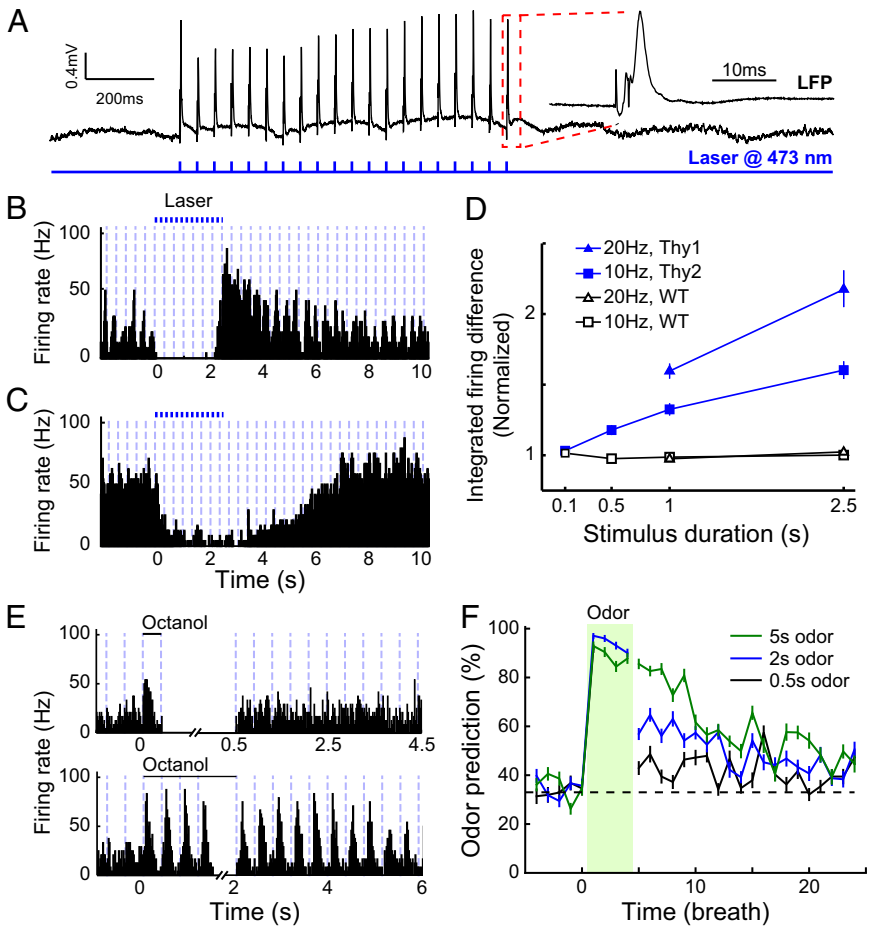

Fig. 8. Increasing stimulus strength drives more persistent network activity. (*A*, *Upper*) LFP recorded in mitral cell layer during Thy1-ChR2 stimulation at 20 Hz. (*Lower*) Light stimulation pulses. (*B*) PSTH from an M/T cell in a Thy1-ChR2 mouse during photostimulation at 20 Hz (bin = 20 ms). After stimulation, this cell was excited for a few seconds. (*C*) PSTH from an M/T cell that was inhibited after Thy1-ChR2 photostimulation. (*D*) Plot of integrated firing difference versus ChR2 stimulus duration (mean ± SEM) for Thy1-ChR2 mice (filled symbols) and WT mice (open symbols). Increasing the length or frequency of photostimulation increased the persistent activity for Thy1-ChR2 mice. $n = 118$ cells from five mice for Thy1-ChR2; 61 cells from two mice for WT. (*E*) PSTHs from one M/T cell from an awake mouse responding to short (0.5 s, *Upper*) and long (2 s, *Lower*) odor presentation (bin = 20 ms). The short presentation did not elicit a postodor response whereas the long presentation did (KS, $P < 0.02$). (*F*) Odor prediction following different odor duration (mean ± SEM of 50 bootstraps, chance level = 33%). Longer stimulus presentations elicited more accurate odor predictions ($n = 81$ cells from three mice).

with each breath in awake mammals. We recorded from M/T cells in awake, head-fixed mice and found that the odor code is dynamic during and after the odor. Between the first and second breath, individual cells could switch from inhibition to excitation, vice versa, or could shift the phase of their response (Fig. 1). On the population level, these differences mean that the odor code for the first breath is different from subsequent breaths (Fig. 2). After odor cessation, we identified an olfactory afterimage that contains odor- and concentration-specific information (Fig. 4) that also depends on stimulus duration (Fig. 8). Using calcium imaging and channelrhodopsin stimulation, we identified the primary site of the odor afterimage as central rather than peripheral (Figs. 6–8). The existence of olfactory afterimages shows that sensory afterimages are common to all sensory systems and may reflect that afterimages serve a functional purpose.

Dynamics of the Odor Response. Some forms of olfactory dynamics have been observed before. In invertebrates, odors elicit complex temporal patterns (43, 44) that stabilize over time (10, 11). In contrast to the gradual changes observed in invertebrates, we observed an abrupt change in the representation between the first and second breath. This disparity may be due to the differences in the way invertebrates and mammals segment olfactory information: by motion and breaths, respectively. Turning to mammals, in anesthetized mice, our laboratory has previously reported that the population representation, using average firing rates, is most in flux at odor onset and offset but did not consider whether these dynamics contained odor information, or the source of these changes (33). We have extended those findings here to awake mice, single cells, and consideration of complex responses not reflected by the average firing rate, and have investigated the source of these dynamics. In the OB of rabbits, and the piriform cortex of anesthetized rats, attenuation has been observed (24, 25, 45). In contrast, we observe many forms of changes between the first and second breath. We should note that we have imaged only the dorsal OB and recorded from medial and dorsal OB, leaving open the possibility that activity is different in the ventral or lateral OB.

Multiple mechanisms could underlie the change in odor code between breaths. Recordings from drosophila and rat ORNs exhibit complex activity patterns, including adaptation, and delayed excitation (14, 46, 47). Imaging of glomeruli shows adaptation (Fig. 5) (15). One simple hypothesis would be that adaptation of ORNs would delay firing downstream. We found that some M/T-cell responses did shift to a later phase during the second breath (Fig. 1*F*), which could reflect attenuation of ORN input. Simple sensory adaptation, however, cannot explain the more dramatic changes in firing after the first breath (Fig. 1*D*).

Feedback within the OB or from higher areas could alter the response after the first breath. M/T cells form dendrodendritic synapses with GABAergic cells, including periglomerular and granule cells, which could mediate feedback within the bulb (48, 49). Besides synapses in the OB, granule cells also receive feedback from higher areas like piriform cortex and the anterior olfactory nucleus (41, 50–52). Given that the largest changes we see are between the first and second breath, it is possible that, before the first breath, the network is at rest; the first breath then activates the olfactory network, including feedback within the OB, and from cortex; then, during the second breath, ORN input is arriving into a different, active network. The delayed LFP activity in the blocked nostril condition (Fig. 7) may reflect the feedback delay. It has been shown that tufted cells are active earlier in the breathing cycle than mitral cells (53, 54); thus, the delayed activity in the blocked nostril condition could reflect that there are two olfactory processing streams, with tufted cells feeding direct olfactory information whereas mitral cells project to recurrent networks. Of note, this feedback appears to be automatic, and independent of attention, as we observed interbreath dynamics in both awake and anesthetized animals. Further experiments using transgenic mice to target granule cells or higher feedback areas will be necessary to isolate the source of the interbreath dynamics.

What cognitive use could this coding shift be useful for? Odor detection and discrimination can occur within a single breath (16, 19–21), and some have hypothesized that subsequent breaths are used for finer discrimination, as a speed–accuracy tradeoff (19, 20). From this view, one might hypothesize that the changes in the odor representation reflect better discriminability between odors; however, in our data, the best odor discrimination was during the first breath. Animals perceive odors clearly only for a few breaths (55), which may be due to the adaptation (not attenuation) that we observe after the first breath. This adaptation may then allow the detection of new odors in the background of the known odor. However, the significant change in representation between the first and second breath raises the issue of how the odor identity can be maintained between the breaths (56) although maintenance of odor identity is not a problem for differences in concentration (27).

The Olfactory Afterimage. Following odor cessation, we recorded odor- and concentration-specific responses that we call an olfactory afterimage. The postodor responses during the first couple of breaths may be due to lingering odorants at low concentrations, but the odors quickly dissipate (Fig. S2). All of our single-cell analyses were performed using the fourth postodor breath, after the odor had gone; furthermore, the postodor prediction was above chance for >10 breaths, long after the odor was gone.

An excitatory persistent afterdischarge that lasts for tens of seconds has previously been reported in the M/T cells of anesthetized mice following odor presentation at 25–50% dilution (12), and short off-responses have been observed in frogs and hamsters (29, 57). In comparison, we observe varied postodor responses including phase changes and inhibition, and our olfactory afterimage lasts only a few seconds. We have furthermore extended the findings to awake mice and odor concentrations two orders of magnitude smaller, showing that the olfactory afterimage contains both odor- and concentration-specific information and is generated centrally.

Where is the olfactory afterimage maintained? The simplest explanation would be continued activity coming from ORNs. Some ORNs in flies have "ultra-prolonged" responses and continue firing seconds after the odor is gone (47, 58). However, when we performed calcium imaging of glomeruli in awake mice, only a small minority of glomeruli were active following the odor, which did not provide enough odor-specific information for classification (Fig. 5). Two-photon calcium imaging in dendritic tufts of mitral cells in anesthetized mice revealed that the calcium activity continues at a low level after odor cessation (59). These findings do not preclude ORN input from contributing to the afterimage but mean that whatever ORN input remains is at a low level.

Multiple lines of evidence point to a central representation. First, we observed that the olfactory afterimage is state-dependent for it is both stronger and longer in awake mice than anesthetized mice. Whether this difference is due to top-down processes like attention or anesthesia-induced changes in the network (28, 32) is impossible to disambiguate. We also observed that the olfactory afterimage is stronger in anesthetized mice for familiar odors over naïve odors although this effect was weak. The second argument for a central representation is that we observed activity in the olfactory bulb in the absence of direct olfactory input, even during the postodor period, which shows that there is feedback from higher areas (41, 52).

The final argument in favor of a central representation is that we were able to induce long-lasting activity in the olfactory network by photostimulating M/T cells with channelrhodopsin. Thy1 is expressed by mitral cells in the bulb (42), and stimulating them simultaneously should induce coactivation of granule cells, as well as activity in the contralateral olfactory bulb, AON, and

piriform cortex. Our recording site in the medial bulb was >1 mm away from the fiber on the dorsal surface, showing that the network is not local. However, not all cells were affected by light stimulation (Fig. S5*A*), which could reflect input specificity to the dorsal bulb stimulation, or that only a subpopulation of cells are influenced by feedback. The observation that increasing light stimulation or odor presentation both yield longer aftereffects may reflect that the network is being driven into a dynamic steady state, which the network has to return from (10). The ChR2-induced activity lasted for >10 breaths and was stronger following prolonged light stimulation; similarly, the olfactory afterimage lasted for >10 breaths and was stronger following longer odor stimulation. The olfactory afterimage could be maintained by the same networks that shape interbreath dynamics. Further experiments targeting specific subpopulations will be necessary to dissect this circuit.

Sensory aftereffects have been observed in all sensory systems and have been most investigated in the visual system, including negative afterimages, the tilt aftereffect, and the motion aftereffect (1, 3, 60). Afterimages are distinguished from aftereffects by the fact that afterimages do not require a second stimulation to reveal their presence; given this definition, we refer to the postodor representations as afterimages. Intricate models have been proposed for the centrally maintained aftereffects, which rely on retinotopy and orientation maps in visual cortex, but olfactory networks lack such organization. The simplest model for visual aftereffects is that central neurons adapt to stimulation of their preferred orientation or direction (61). Although some cells did adapt during the odor (Figs. 1*C* and 3*D*), the postodor responses were too diverse for simple adaptation to explain the olfactory afterimage. Thus, central olfactory afterimages are likely maintained by olfaction-specific network properties.

The long duration and odor specificity of the olfactory afterimages lead us to hypothesize that they are a form of short-term memory (62). What is intriguing about this sensory memory is that there has been no report of a perceptual analog: that is, odor perception in the absence of odor. (It is difficult to design a behavioral paradigm to test postodor discrimination without the confound of odor discrimination.) In contrast, stimulus aftereffects in vision and audition are typically associated with perceptual analogs. This olfactory memory could be useful in contexts where an animal encounters multiple different odorants in a time-varying fashion and needs to distinguish between familiar and novel odorants.

Materials and Methods

For details, see *SI Materials and Methods*.

Animals. For electrophysiology, we recorded from seven Slc6a4-Cre heterozygous mice in a C57BL/6J background, sixteen C57BL/6J mice, and five Thy1-ChR2 mice (*B6.Cg-Tg(Thy1-ChR2/EYFP)*^{18Gfng}*/J*, JAX 007612; The Jackson Laboratory). All mice were male, with the exception of two Thy1-ChR2 mice. Slc6a4-Cre (GENSAT) mice were infected with floxed-ChR2-YFP injected in the Raphe, but recordings were performed before photostimulation. All animals recorded were >8 wk old and maintained in 12-h day/night cycle. For calcium imaging, we used floxed-GCaMP3/OMP-Cre mice [*Gt(ROSA) 26Sor*$^{tm38(CAG-GCaMP3)Hze}$*/J* (63): JAX 014538, crossed with *OMP*$^{tm4(cre)Mom}$ (64); JAX 006668] in a C57BL/6J background, hemizygous for both alleles, and imaged at 6–7 wk old. All animal protocols were in accordance with the Swiss Federal Act on Animal Protection and the Swiss Animal Protection Ordinance and were approved by the University of Geneva and Geneva state ethics committees (authorization 1007/3387/2).

Surgery and Recording. Steel head-posts were cemented to the mice's skulls 2–3 d before recording. Mice were then habituated to the recording apparatus for 2–3 training sessions before recording. We used silicon-based recording electrodes (A-4 × 2-Tet-5 mm-150–200-312; NeuroNexusTech) for extracellular recordings acquired at 32 kHz, and transferred to computers via DigitalLynx (Neuralynx). For calcium imaging, we thinned the skull over the olfactory bulb and placed a 5-mm coverglass over it. Images were acquired at 50 Hz for 10 s using a Micam Ultima system (Brainvision) mounted on a custom-built microscope (65). We presented odors using a custom-made olfactometer, coordinated via computer, as described previously (33, 65). For details of surgery, electrophysiology, calcium imaging, and detailed analysis, see *SI Materials and Methods*.

ACKNOWLEDGMENTS. We are grateful to Anthony Holtmaat for providing Thy1-ChR2 mice and to Richard Benton for technical assistance with the miniPID. We thank Ian Davison, Ivan Rodriguez, and members of the A.C. laboratory for helpful discussions and comments on the manuscript. This work was supported by the University of Geneva, the Swiss National Science Foundation (SNF Professor Grants PP0033_119169 and PP00P3_139189), the European Research Council (Contract ERC-2009-StG-243344-NEUROCHEMS), the National Center of Competence in Research project "SYNAPSY: The Synaptic Bases of Mental Diseases" financed by the Swiss National Science Foundation (51AU40_125759), the Novartis Foundation for Medical Research, the Carlos and Elsie de Reuter Foundation, the Ernst and Lucie Schmidheiny Foundation, and the European Molecular Biology Organization (Young Investigator Program).

1. Krekelberg B, Boynton GM, van Wezel RJ (2006) Adaptation: From single cells to BOLD signals. *Trends Neurosci* 29(5):250–256.
2. Wilson RI, Mainen ZF (2006) Early events in olfactory processing. *Annu Rev Neurosci* 29:163–201.
3. Mather G, Pavan A, Campana G, Casco C (2008) The motion aftereffect reloaded. *Trends Cogn Sci* 12(12):481–487.
4. Zwicker E (1964) "Negative afterimage" in hearing. *J Acoust Soc Am* 36:2413.
5. Hoke ES, Hoke M, Ross B (1996) Neurophysiological correlate of the auditory afterimage ("Zwicker tone"). *Audiol Neurootol* 1(3):161–174.
6. Vogels IM, Kappers AM, Koenderink JJ (1996) Haptic aftereffect of curved surfaces. *Perception* 25(1):109–119.
7. Petreanu L, et al. (2012) Activity in motor-sensory projections reveals distributed coding in somatosensation. *Nature* 489(7415):299–303.
8. James GA, Li X, DuBois GE, Zhou L, Hu XP (2009) Prolonged insula activation during perception of aftertaste. *Neuroreport* 20(3):245–250.
9. Schiffman SS, Reilly DA, Clark TB III, (1979) Qualitative differences among sweeteners. *Physiol Behav* 23(1):1–9.
10. Mazor O, Laurent G (2005) Transient dynamics versus fixed points in odor representations by locust antennal lobe projection neurons. *Neuron* 48(4):661–673.
11. Brown SL, Joseph J, Stopfer M (2005) Encoding a temporally structured stimulus with a temporally structured neural representation. *Nat Neurosci* 8(11):1568–1576.
12. Matsumoto H, Kashiwadani H, Nagao H, Aiba A, Mori K (2009) Odor-induced persistent discharge of mitral cells in the mouse olfactory bulb. *J Neurophysiol* 101(4):1890–1900.
13. Verhagen JV, Wesson DW, Netoff TI, White JA, Wachowiak M (2007) Sniffing controls an adaptive filter of sensory input to the olfactory bulb. *Nat Neurosci* 10(5):631–639.
14. Rospars J-P, Lansky P, Chaput M, Duchamp-Viret P (2008) Competitive and noncompetitive odorant interactions in the early neural coding of odorant mixtures. *J Neurosci* 28(10):2659–2666.
15. Spors H, Grinvald A (2002) Spatio-temporal dynamics of odor representations in the mammalian olfactory bulb. *Neuron* 34(2):301–315.
16. Cury KM, Uchida N (2010) Robust odor coding via inhalation-coupled transient activity in the mammalian olfactory bulb. *Neuron* 68(3):570–585.
17. Shusterman R, Smear MC, Koulakov AA, Rinberg D (2011) Precise olfactory responses tile the sniff cycle. *Nat Neurosci* 14(8):1039–1044.
18. Gschwend O, Beroud J, Carleton A (2012) Encoding odorant identity by spiking packets of rate-invariant neurons in awake mice. *PLoS ONE* 7(1):e30155.
19. Rinberg D, Koulakov A, Gelperin A (2006) Speed-accuracy tradeoff in olfaction. *Neuron* 51(3):351–358.
20. Abraham NM, et al. (2004) Maintaining accuracy at the expense of speed: Stimulus similarity defines odor discrimination time in mice. *Neuron* 44(5):865–876.
21. Uchida N, Mainen ZF (2003) Speed and accuracy of olfactory discrimination in the rat. *Nat Neurosci* 6(11):1224–1229.
22. Miura K, Mainen ZF, Uchida N (2012) Odor representations in olfactory cortex: Distributed rate coding and decorrelated population activity. *Neuron* 74(6):1087–1098.
23. Poo C, Isaacson JS (2009) Odor representations in olfactory cortex: "Sparse" coding, global inhibition, and oscillations. *Neuron* 62(6):850–861.
24. Kadohisa M, Wilson DA (2006) Olfactory cortical adaptation facilitates detection of odors against background. *J Neurophysiol* 95(3):1888–1896.
25. Best AR, Wilson DA (2004) Coordinate synaptic mechanisms contributing to olfactory cortical adaptation. *J Neurosci* 24(3):652–660.
26. Slotnick BM, Ptak JE (1977) Olfactory intensity-difference thresholds in rats and humans. *Physiol Behav* 19(6):795–802.
27. Stopfer M, Jayaraman V, Laurent G (2003) Intensity versus identity coding in an olfactory system. *Neuron* 39(6):991–1004.
28. Vincis R, Gschwend O, Bhaukaurally K, Beroud J, Carleton A (2012) Dense representation of natural odorants in the mouse olfactory bulb. *Nat Neurosci* 15(4):537–539.

29. Meredith M (1986) Patterned response to odor in mammalian olfactory bulb: The influence of intensity. *J Neurophysiol* 56(3):572–597.
30. Rezec A, Krekelberg B, Dobkins KR (2004) Attention enhances adaptability: Evidence from motion adaptation experiments. *Vision Res* 44(26):3035–3044.
31. Chaudhuri A (1990) Modulation of the motion aftereffect by selective attention. *Nature* 344(6261):60–62.
32. Kato HK, Chu MW, Isaacson JS, Komiyama T (2012) Dynamic sensory representations in the olfactory bulb: Modulation by wakefulness and experience. *Neuron* 76(5): 962–975.
33. Bathellier B, Buhl DL, Accolla R, Carleton A (2008) Dynamic ensemble odor coding in the mammalian olfactory bulb: Sensory information at different timescales. *Neuron* 57(4):586–598.
34. Rojas-Líbano D, Kay LM (2012) Interplay between sniffing and odorant sorptive properties in the rat. *J Neurosci* 32:15577–15589.
35. Cenier T, McGann JP, Tsuno Y, Verhagen JV, Wachowiak M (2013) Testing the sorption hypothesis in olfaction: A limited role for sniff strength in shaping primary odor representations during behavior. *J Neurosci* 33(1):79–92.
36. Gautam SH, Verhagen J V (2012) Retronasal odor representations in the dorsal olfactory bulb of rats. *J Neurosci* 32:7949–7959.
37. Philpot BD, Foster TC, Brunjes PC (1997) Mitral/tufted cell activity is attenuated and becomes uncoupled from respiration following naris closure. *J Neurobiol* 33(4): 374–386.
38. Kikuta S, Kashiwadani H, Mori K (2008) Compensatory rapid switching of binasal inputs in the olfactory cortex. *J Neurosci* 28(46):11989–11997.
39. Neville KR, Haberly LB (2003) Beta and gamma oscillations in the olfactory system of the urethane-anesthetized rat. *J Neurophysiol* 90(6):3921–3930.
40. Kay LM, et al. (2009) Olfactory oscillations: The what, how and what for. *Trends Neurosci* 32(4):207–214.
41. Boyd AM, Sturgill JF, Poo C, Isaacson JS (2012) Cortical feedback control of olfactory bulb circuits. *Neuron* 76(6):1161–1174.
42. Arenkiel BR, et al. (2007) In vivo light-induced activation of neural circuitry in transgenic mice expressing channelrhodopsin-2. *Neuron* 54(2):205–218.
43. Laurent G, Wehr M, Davidowitz H (1996) Temporal representations of odors in an olfactory network. *J Neurosci* 16(12):3837–3847.
44. Friedrich RW, Laurent G (2001) Dynamic optimization of odor representations by slow temporal patterning of mitral cell activity. *Science* 291(5505):889–894.
45. Chaput MA, Panhuber H (1982) Effects of long duration odor exposure on the unit activity of olfactory bulb cells in awake rabbits. *Brain Res* 250(1):41–52.
46. Kreher SA, Kwon JY, Carlson JR (2005) The molecular basis of odor coding in the Drosophila larva. *Neuron* 46(3):445–456.
47. Montague SA, Mathew D, Carlson JR (2011) Similar odorants elicit different behavioral and physiological responses, some supersustained. *J Neurosci* 31(21): 7891–7899.
48. Schoppa NE, Urban NN (2003) Dendritic processing within olfactory bulb circuits. *Trends Neurosci* 26(9):501–506.
49. Isaacson JS (2010) Odor representations in mammalian cortical circuits. *Curr Opin Neurobiol* 20(3):328–331.
50. Strowbridge BW (2009) Role of cortical feedback in regulating inhibitory microcircuits. *Ann N Y Acad Sci* 1170:270–274.
51. Gao Y, Strowbridge BW (2009) Long-term plasticity of excitatory inputs to granule cells in the rat olfactory bulb. *Nat Neurosci* 12(6):731–733.
52. Markopoulos F, Rokni D, Gire DH, Murthy VN (2012) Functional properties of cortical feedback projections to the olfactory bulb. *Neuron* 76(6):1175–1188.
53. Fukunaga I, Berning M, Kollo M, Schmaltz A, Schaefer ATT (2012) Two distinct channels of olfactory bulb output. *Neuron* 75(2):320–329.
54. Igarashi KM, et al. (2012) Parallel mitral and tufted cell pathways route distinct odor information to different targets in the olfactory cortex. *J Neurosci* 32(23):7970–7985.
55. Dalton P (2000) Psychophysical and behavioral characteristics of olfactory adaptation. *Chem Senses* 25(4):487–492.
56. Gottfried JA (2010) Central mechanisms of odour object perception. *Nat Rev Neurosci* 11(9):628–641.
57. Kauer JS (1974) Response patterns of amphibian olfactory bulb neurones to odour stimulation. *J Physiol* 243(3):695–715.
58. Turner SL, et al. (2011) Ultra-prolonged activation of CO2-sensing neurons disorients mosquitoes. *Nature* 474(7349):87–91.
59. Charpak S, Mertz J, Beaurepaire E, Moreaux L, Delaney K (2001) Odor-evoked calcium signals in dendrites of rat mitral cells. *Proc Natl Acad Sci USA* 98(3):1230–1234.
60. Kohn A (2007) Visual adaptation: Physiology, mechanisms, and functional benefits. *J Neurophysiol* 97(5):3155–3164.
61. Huk AC, Ress D, Heeger DJ (2001) Neuronal basis of the motion aftereffect reconsidered. *Neuron* 32(1):161–72.
62. Galán RF, Weidert M, Menzel R, Herz AV, Galizia CG (2006) Sensory memory for odors is encoded in spontaneous correlated activity between olfactory glomeruli. *Neural Comput* 18(1):10–25.
63. Zariwala HA, et al. (2012) A Cre-dependent GCaMP3 reporter mouse for neuronal imaging in vivo. *J Neurosci* 32(9):3131–3141.
64. Li J, Ishii T, Feinstein P, Mombaerts P (2004) Odorant receptor gene choice is reset by nuclear transfer from mouse olfactory sensory neurons. *Nature* 428(6981):393–399.
65. Bathellier B, Van De Ville D, Blu T, Unser M, Carleton A (2007) Wavelet-based multiresolution statistics for optical imaging signals: Application to automated detection of odour activated glomeruli in the mouse olfactory bulb. *Neuroimage* 34(3): 1020–1035.

Supporting Information

Patterson et al. 10.1073/pnas.1303873110

SI Materials and Methods

Surgery and Electrophysiology. We attached steel head-posts to the mice 2–14 d before recording, under isofluorane anesthesia, using Syntac dental adhesive and Miris 2 Dentin dental cement (Ivoclar Vivadent). Starting 2–3 d before recording, animals were acclimated to the head restraint during 30- to 60-min sessions to reduce stress and movement. On the day of recording, mice were anesthetized with isoflurane and head-restrained. The skull over the olfactory bulb was thinned via dentral drill and removed using a bent 26G needle, as well as the dura. We recorded from the olfactory bulb (OB) using 32-channel silicon probes (NeuroNexusTech; A4 × 2-tet-5 mm-150–200-312-A32). Once the tetrodes were in the brain, electrical contact was maintained with a ground wire via LacryVisc (Alcon), as it evaporates slower than artificial cerebral spinal fluid (ACSF). Electrodes penetrated the brain at an angle, and we recorded from the dorsal and medial surfaces. Mitral/tufted (M/T) cells were identified as described previously (1). While searching for M/T cells, the tetrodes were stepped by 2.5 μm. We often stopped for 5–10 min to let the brain rebound from penetration, and immediately before recording. Typical recording sessions lasted 3 to 4 h and included recording from two to four sites, along two electrode penetrations. Recordings were abbreviated if the mice persistently moved or made vocalizations.

Recordings were acquired at 32 kHz, transferred to computer via DigitalLynx (Neuralynx), and bandpass filtered between 1 and 9,000 Hz. Following the experiment, we used the NDManager suite of software (2) to filter and extract spikes. The software automatically median-subtraction filtered recordings (filter size, 1 ms), detected the baseline noise in each channel, and determined the threshold for spike detection. As users, we modified a small number of parameters, including filter width, spike detection window width, and the threshold for spike detection. Following spike extraction, the software calculated the principal components of each spike waveform, using the voltage from all channels from a tetrode, and clustered spikes using an expectation minimization algorithm. After clustering, units were manually verified to have consistent spike waveforms on all electrodes, to be present for a whole experiment, and to have a U-shaped autocorrelation histogram.

For the blocked-nostril experiments, we applied a silicon elastomer (World Precision Instruments; Kwik-Cast) liberally over the naris. Mice were anesthetized to prevent them from relieving the blockage. When we removed the plastic during the experiment, we verified that the plastic molded to the inside of the nasal cavity, to ensure complete blockage. Upon removal of the plastic, the respiratory pressure in the contralateral nostril halved (Fig. 6). To ensure that the local field potential (LFP) was measured in the mitral cell layer, LFPs were recorded from tetrodes that included spikes; to avoid contamination by spikes, the LFP was measured from neighboring, nonspiking electrodes.

For the Thy1-ChR2 experiments, we placed a light fiber (200 μm diameter, BFL37-200; Thorlabs) over the dorsal OB and controlled stimulation via an MP-285. Light was supplied by a 473-nm laser (Shanghai Dream Laser; SDL-473–050MFL), and, before each experiment, we verified the power was 10–15 mW.

Odor Delivery. All odors (Table S1) were from Sigma-Aldrich. Odors were replaced weekly and checked for viability before each experiment. During experiments, we chose three odors from the above set and presented them for 10–12 trials. We presented odors using a custom-made olfactometer, coordinated via computer (1). To prevent odor leakage, the olfactometer constantly aspirated, except during odor presentation. To mix odors, a carrier flow passed through small bottles containing 3 mL of pure odorant, and diluted to 5% in clean dry air for 2 s to allow for equilibration. For lower concentrations (0.1–2%), the odorants were first diluted 1:10 in mineral oil and then diluted further by air. Odors were presented for 2 or 2.5 s (0.4 L/min) to the left nostril in a pseudorandom pattern (unless otherwise stated). The delay between valve opening and odor arrival at the nostril was 22 ms. Following odor offset, the olfactometer paused 2 s and then purged all odor lines (while under constant aspiration). Given computer delays, the intertrial interval was 12–15 s. Respiration was detected via a directional airflow sensor (Honeywell; AWM2100V) near the contralateral nostril. To present odors between inspirations, a window discriminator detected the end of inspiration, at which time the aspiration turned off, allowing the odor to flow.

We used a photoionization detector (PID) (Aurora Scientific, 200B miniPID) to measure the odor concentration during and after the odor. The PID was placed 5 mm from the odor nozzle and allowed to warm up 30 min. Odors were presented for 10 trials, and the voltage output of the PID recorded with a sampling rate of 1 kHz.

Calcium Imaging. The day of the recording, we anesthetized the OMP-GCaMP3 mice with isoflurane while maintaining the body temperature. We removed the skin over both olfactory bulbs under local anesthesia using carbostesin (AstraZeneca) and thinned the skull with a scalpel blade to allow light transmission. A drop of ACSF buffer was placed on top of the thinned bone and covered with a 5-mm coverglass. Following surgery, the animal recovered from anesthesia while being head-fixed under the microscope.

Images (100 × 100 pixels) were acquired at 50 Hz for 10 s using a Micam Ultima system (Brainvision) mounted on a custom-built microscope (Navitar 17 mm, bottom lens, Nikon 135 mm, upper lens; total magnification 7.9×). The olfactory bulb was illuminated with a 480-nm light (filter HQ 480/40), reflected to the brain by a dichroic mirror (Q 505 LP). Emitted light passed through a 535-nm band pass filter (HQ 535/50). The light intensity was adjusted to have an average resting fluorescence at 20% of the sensitivity of our camera. No significant bleaching was observed with these settings.

The odorants (Table S1) were presented for at least eight trials and delivered for 3 s. Most odorants were diluted 20× in air; some odorants that elicited weak maps on the dorsal surface (e.g., limonene or propanediol) were diluted at up to 2× in air. All fluorescence data are expressed as ΔF/F relative to the resting fluorescence (F_0) averaged over 1.2 s before the odor delivery. To remove motion artifacts, we subtracted an averaged temporal profile, calculated using a mask excluding glomeruli that had a significant odor response and excluding the lateral half of the image from each pixel's time course. The average breath duration was calculated and used to extract single-breath data from the calcium imaging data. Four breaths before the stimulus, 6 during the odor, and 11 after the odor were taken into account. To identify responsive glomeruli, for each breath, the amplitude of the fluorescence signal, averaged over a given region of interest (ROI), was calculated on the smoothed trace (running average, 100 ms width). Those ROIs, which had a ΔF/F more than four times the SD during the baseline (for that ROI), were considered responsive. A single exponential fit was removed from the postodor data to calculate the breath modulation.

Single Cell Statistics. Because timing during the breathing cycle is critical, we aligned all spikes to the start of the breathing cycle (3). To standardize breathing cycles, we truncated all spikes that occurred after the end of the mean breath duration and padded short breaths with empty time. The alignment was done to allow comparison between different length breaths, but maintaining spike timing following inspiration, which is how most olfactory information is encoded in the bulb (1, 4, 5). The mice often "fast-breathed" during the first and second trials, which we elided from analysis. The odor concentration also took some time to stabilize (Fig. S1). Given this stabilization time, we also removed trials where the first breath was less than 150 ms after odor presentation started.

To determine whether a cell–odor pair responded to the odor, we calculated its "rate" and "temporal" response statistics. For postodor responses, given that it takes a few hundred milliseconds for the odor to dissipate, we used the fourth postodor breath. To detect rate responses (changes in average firing rate during the breath), we calculated the average firing rate over the entire breath for five preodor breaths, first five odor breaths, and postodor breaths 4–6. Differences were tested via one-way ANOVA and post hoc tested with Tukey's t test. To detect temporal responses, we calculated the cumulative distribution of spikes during preodor, odor, and postodor breathing cycles and then tested for difference between them using the Kolmogorov–Smirnov (KS) test (4). Given the large number of KS tests, we performed a calibration by comparing two preodor control breaths for each cell recorded. We found that, with a KS criterion of $P < 0.02$, less than 5% of preodor control breaths were identified as significantly different from each other. For cells identified as having temporal responses, we assumed the breathing cycle had a circular distribution and calculated the circular mean (i.e., the phase) and circular variance (magnitude of phasing using a circular statistics package for MATLAB (6), as we have done previously (1). This phase analysis yielded a simple quantification of the phase of responses that could include both excitation and inhibition in the same measure.

Population Representations. To look at interbreath changes in the population representation, we built population vectors as shown in Fig. 2*A*. For each cell, we binned the spikes during each breath into 8 bins (~40 ms; similar results were obtained using 16 bins) and then built a population vector including the entire breathing cycle for each cell. To increase the contrast for the breath-distance calculation, we performed principal component analysis (PCA) on the average population vector (results using simple spike distance were similar, with a smaller magnitude). Using the PCA population vector, we calculated the mean distance between four preodor breaths to get a baseline for the variability (Δ_{ctl}). Then, for a given odor, we calculated the distances between the average preodor breath, and the first five odor-breaths Δ_{0-5}, and normalized to the preodor distance ($\Delta_{0-5}/\Delta_{ctl}$). To get the average distance, we averaged the results from six recordings from five animals, where each recording had 13 or more cells.

For the odor prediction, we used a template-matching algorithm (1, 3). We used the same population vector as we used for the breath distance calculation, but, instead of calculating distances between breaths of the same odor, we calculated distances between odors during the same breath. For each breath of each trial, we built a population vector of the response during the trial for each odor "o" ($r_{o,sample}$) and the average response during other trials ($r_{o,template}$) and then calculated the distance between each sample and the template for each odor ($r_{o,sample} - r_{o,template}$), with the minimum distance being the classified odor. Normally the sample and template were selected from the same breath (Figs. 2*C*, 3*G*, 4*C*, 5*E*, and 8*F*). For some experiments, to investigate dynamics, we compared the samples from each breath to a template from a fixed breath (Fig. 2C and Figs. S2*C* and S4*B*). To select trials and cells for the population vector, we used a bootstrap approach, selecting ten trials, and ~50–60 cells (with replication). Results were then averaged over 50 iterations. Here, the accuracy was high enough that we used simple spike distance rather than the PCA representation.

To calculate the integrated firing distance, we created a response profile for each breath by calculating the average spike count in 16 bins (~20 ms). Then, we summed the difference between the prelight and postlight profiles for each breath and normalized to the difference between control breaths. Using this technique, there was no correlation between the firing rate of a neuron and the integrated difference (Fig. S5*B*). As an alternative, we normalized the integrated difference to the firing rates of the neurons and obtained similar results (Fig. S5*C*), but these results had a strong inverse relationship between the firing rate of neurons and the changes in firing (Fig. S5*D*). For Fig. 8*D*, we summed the differences of the first five breaths.

1. Bathellier B, Buhl DL, Accolla R, Carleton A (2008) Dynamic ensemble odor coding in the mammalian olfactory bulb: Sensory information at different timescales. *Neuron* 57(4):586–598.
2. Hazan L, Zugaro M, Buzsáki G (2006) Klusters, NeuroScope, NDManager: A free software suite for neurophysiological data processing and visualization. *J Neurosci Methods* 155(2):207–216.
3. Gschwend O, Beroud J, Carleton A (2012) Encoding odorant identity by spiking packets of rate-invariant neurons in awake mice. *PLoS ONE* 7(1):e30155.
4. Cury KM, Uchida N (2010) Robust odor coding via inhalation-coupled transient activity in the mammalian olfactory bulb. *Neuron* 68(3):570–585.
5. Carey RM, Wachowiak M (2011) Effect of sniffing on the temporal structure of mitral/tufted cell output from the olfactory bulb. *J Neurosci* 31:10615–10626.
6. Berens P (2009) CircStat: A MATLAB toolbox for circular statistics. *J Stat Softw* 31(10):1–21.

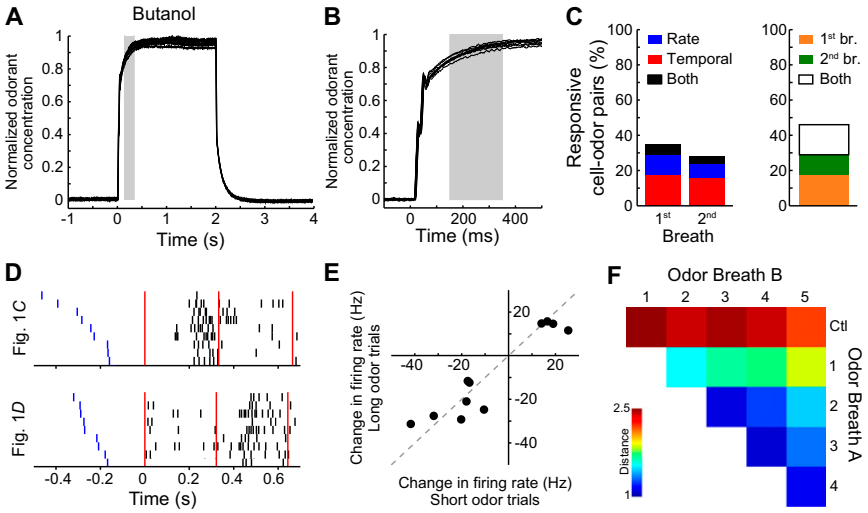

Fig. S1. PID measurements. (*A*) Output of miniPID for 10 trials during presentation of Butanol. The odor concentration quickly reaches 85% of the maximum concentration and then increases to 100% after a few hundred milliseconds. The range of time for the first breath is shown in gray. All odorants had similar profiles. The mean variance between trials was ± 2.5% ($n = 15$ measurements). (*B*) Expanded timescale of the odor onset. Odor presentation is initiated by the end of aspiration, and it takes ~20 ms from the odor pulse trigger for the release of negative pressure to reach the odor nozzle. The odor concentration rapidly increases over 50 ms and then increases gradually. The intertrial variance was similar to the increase in concentration between breaths. (*C*) The percentage of responsive cells following recording with the miniPID ($n = 728$ odor-cell pairs, seven odors, three mice). The 64/231 cell–odor pairs that had a temporal response during the first breath changed their response during the second breath (KS test, $P < 0.02$). (*D*) We wondered whether the changes between the first and second breath were due to the small changes in concentration during the beginning of the odor presentation, rather than neuronal process. Given that odor concentration increases 5–10% during the period of the first breath (similar to the changes between the first and second breath), we used the duration of odor presentation as a proxy for small changes in concentration and investigated cells that had large changes in firing rate between the first and second breath (>10 Hz). Shown here are raster plots of the responses shown in Fig. 1 *C* and *D*, ordered from shortest odor duration to longest (odor start shown as blue bars to left). For both cells, the responses during the first breath are independent of odor duration. Red bars indicate inspiration onset. (*E*) To quantify this measure for all cells with large changes in firing rate, we calculated the change in firing rate between the first and second breath for the shortest trials and the longest trials (positive numbers indicate an increase in firing rate from the first to second breath). If the changes between the first and second breath were due to concentration changes, one would expect the points to lie closer to the *x* axis. To test concentration hypothesis statistically, we normalized the changes by taking the absolute value, performed a paired *t* test, and found no significant difference between long and short odor trials ($P = 0.48$). (*F*) Breath distance measurement for the recordings with paired PID measurements. The first breath is most different from subsequent breaths.

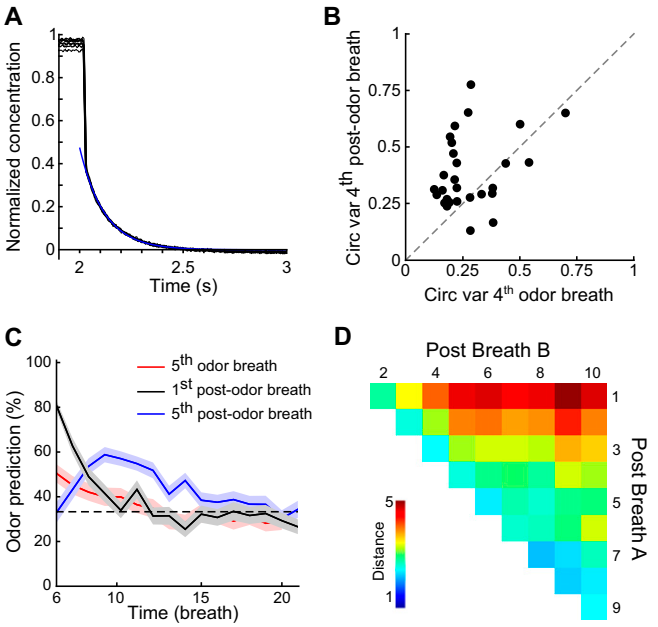

Fig. S2. The postodor representation is dissimilar from the odor and evolves gradually. (*A*) To see whether odors were present after stimulation, we measured the odorant concentration using a PID. In this example, 50 ms after the end of presentation, the concentration dropped to 27% of its initial value (on average, it dropped to 14 ± 6% SD, $n = 15$ measurements). After the initial drop, the concentration decayed rapidly to baseline, which we could fit with a single exponential (tau for this example is 142 ms; average tau = 175 ± 35 ms SD). In some cases, the measured concentration dropped below the background level (as shown here), presumably due to pressure effects. (*B*) Temporal responses were less phasic during the postodor period than during the odor. $n = 22$ cell–odor pairs that fired phasically both during the odor and postodor. (*C*) Postodor prediction using a fixed template from the fifth odor breath (red), first postodor breath (black), or fifth postodor breath (blue). The odor template does not yield a strong prediction. The postodor templates are accurate only for the nearby breaths. Mean ± SEM of 50 permutations, same data set as Fig. 3. (*D*) Spike distance between breaths during the postodor period. The representation changes gradually. Color bar, normalized breath distance.

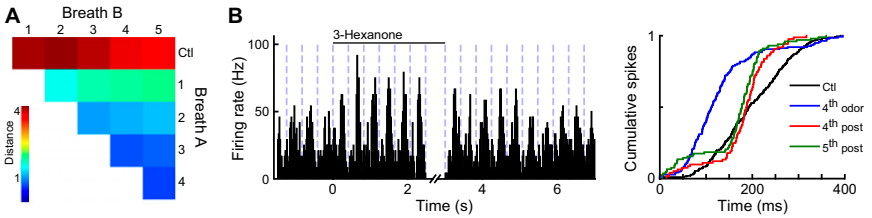

Fig. S3. Odor representations in anesthetized mice are dynamic. (*A*) Breath distance plot during the odor for anesthetized mice. The first odor breath is different from the later odor breaths (ANOVA, $P < 0.05$). Color bar, normalized breath distance. (*B*) Example M/T cell from an anesthetized mouse with postodor response. (*Left*) PSTH binned at 40 ms. (*Right*) Spike distribution during control (black), the fourth odor (blue), and postodor (red, gray) breaths. The postodor response has a different phase than the odor response (KS, $P < 0.02$).

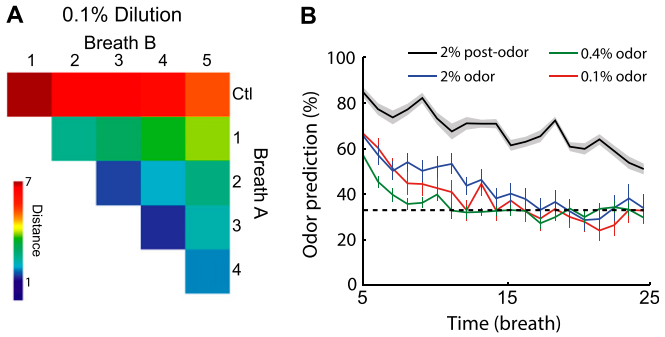

Fig. S4. Breath dynamics at low concentration. (*A*) Interbreath dynamics persist at lower concentrations. To see whether the interbreath odor dynamics observed in Figs. 1 and 2 were due to the high concentration used, we repeated the analysis at a lower concentration. Same dataset as Fig. 4. Results are mean from 50 permutations of ~50 cells. Color bar, normalized breath distance. (*B*) The postodor representation is not similar to low concentrations of the odor. Odor was presented at 2% dilution. The postodor was classified using a template from the same postodor breath (black), or using a template from the fourth odor breath at 2% (blue), 0.4% (green), or 0.1% dilution (red). The predictions using the odor templates fall to chance whereas the postodor prediction remains high. The poor prediction using low-concentration templates implies that the afterimage is not due to low-concentration odorants. Same dataset as Fig. 4.

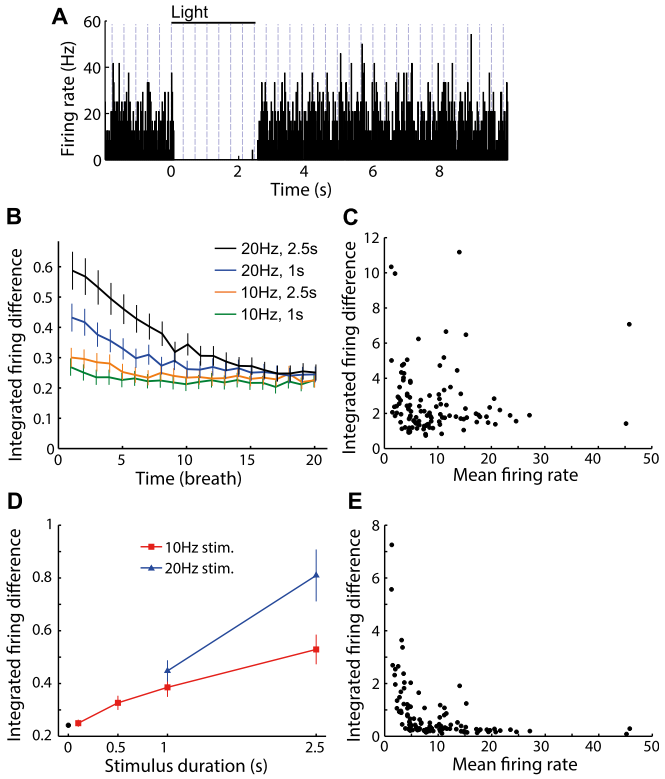

Fig. S5. Thy1-ChR2 stimulation effect dissipates with time. (*A*) PSTH from an M/T cell that did not change its firing after Thy1-ChR2 photostimulation (20 Hz, 2.5 s; 20-ms bins). (*B*) The integrated firing difference for 20 breaths following the termination of Thy1-ChR2 stimulation at 10 Hz (orange, 1 s; green, 2.5 s), and 20 Hz (blue, 1 s; black, 2.5 s). (*C*) Plot of integrated firing difference vs. firing rate for all cells following 20 Hz, 2.5 s of Thy1-Chr2 stimulation. The integrated firing measure, normalized to the preodor difference, is not correlated with the firing rate. (*D*) Normalizing the firing difference simply by the firing rate yields a similar result to normalizing to the preodor difference. The black dot is the difference for five control breaths. (*E*) The integrated firing difference (20 Hz, 2.5 s), normalized to the firing rate, is inversely related to the firing rate.

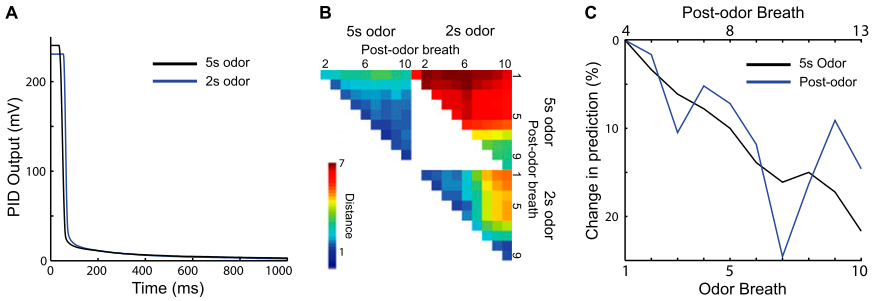

Fig. S6. Stimulation with different odor durations causes different afterimages. (*A*) The output of the PID following 5-s (black) and 2-s (blue) hexanone presentation. The postodor concentration was similar for both durations. (*B*) The postodor representations are different following odor presentation of different lengths. We calculated the distance between breaths (Fig. 2 and *Materials and Methods*) during the postodor period following odor presentation for 2 or 5 s. Comparing the distance between breaths following each odor duration shows a gradual evolution. Comparing the distance between the breaths following different odor duration shows a much larger distance, showing that the representations are different following different length odor presentation. The spike distances were enhanced in PCA space. Color bar, normalized distance. (*C*) The breath-by-breath decrease in information was similar during the odor and the postodor. Shown is the decrease in information from the first breath during 5-s odor stimulation versus the decrease in information from the fourth postodor following 2-s odor stimulation.

Table S1. Odorant properties and sample sizes

Odor	Log(K_{ow})	Log(VP)	Log(Henry)	No. of cells (e-phys)	No. of ROI (imaging)
Amyl acetate	2.3	0.62	−3.3	281	79
Ethyl butyrate	1.9	1.2	−3.4	168	79
3-hexanone	1.5	1.2	−3.9	276	79
1-butanol	0.84	0.9	−5	65	89
1-octanol	3	−1	−4.5	102	89
1,2-propanediol	−0.8	−0.7	−6.8	104	89
Thujopsene	6.1	−1.2	−0.59	104	
Nonanol	4	−1.5	−4.4	104	89
(R)-(+)-limonene	4.8	0.19	−0.42	104	65
Acetoin	−0.36	0.28	−5		89
Hexanal	1.9	0.99	−3.7		89
Methyl benzoate	2	−0.4	−4.5		168
Acetophenone	1.6	−0.48	−5		79
Pentanol	1.4	0.45	−4.9		79

Odorant physicochemical properties and sample sizes used for Fig. 6. Log(K_{ow}), log water–octanol partition. Log(VP), $\log_{10}$ of vapor pressure in mmHg at 25 °C. Log(Henry), $\log_{10}$ of the Henry's law bond constant. All odorant properties were researched on Chemspider, under the EPISuite tab. The sample sizes for electrophysiology and imaging were calculated differently. For electrophysiology, we included all cells that we recorded from, regardless of whether they responded to any odor. For imaging, we can include only ROI that respond to at least one odor, as unresponsive ROI blend into the background.